Robustness of Dynamical Feedbacks from Radiative Forcing: 2% Solar versus 2 × CO_2 Experiments in an Idealized GCM

MING CAI

Department of Earth, Ocean, and Atmospheric Science, Florida State University, Tallahassee, Florida

KA-KIT TUNG

Department of Applied Mathematics, University of Washington, Seattle, Washington

(Manuscript received 29 April 2011, in final form 11 March 2012)

ABSTRACT

Despite the differences in the spatial patterns of the external forcing associated with a doubling CO_2 and with a 2% solar variability, the final responses in the troposphere and at the surface in a three-dimensional general circulation model appear remarkably similar. Various feedback processes are diagnosed and compared using the climate feedback–response analysis method (CFRAM) to understand the mechanisms responsible.

At the surface, solar radiative forcing is stronger in the tropics than at the high latitudes, whereas greenhouse radiative forcing is stronger at high latitudes compared with the tropics. Also solar forcing is positive everywhere in the troposphere and greenhouse radiative forcing is positive mainly in the lower troposphere. The water vapor feedback strengthens the upward-decreasing radiative heating profile in the tropics and the poleward-decreasing radiative heating profile in the lower troposphere. The ''evaporative'' and convective feedbacks play an important role only in the tropics where they act to reduce the warming at the surface and lower troposphere in favor of upper-troposphere warming. Both water vapor feedback and enhancement of convection in the tropics further strengthen the initial poleward-decreasing profile of energy flux convergence perturbations throughout the troposphere. As a result, the large-scale dynamical poleward energy transport, which acts on the negative temperature gradient, is enhanced in both cases, contributing to a polar amplification of warming aloft and a warming reduction in the tropics. The dynamical amplification of polar atmospheric warming also contributes additional warming to the surface below via downward thermal radiation.

1. Introduction

Following the pioneering work of Manabe and Wetherald (1975) and Manabe (1983), Hansen et al. (1984) performed general circulation model (GCM) experiments that include doubling CO_2 and increasing the solar constant by 2%—''forcings of roughly equal magnitude''—to study climate sensitivity. The surface temperature response was found to be remarkably similar in magnitude and in seasonal and meridional variations. This is in spite of the fact that solar radiative heating follows the sun and so has much stronger seasonal and meridional contrasts than the more uniform greenhouse radiative forcing. Both showed larger warming at the polar regions in winter than in summer, and amplified warming at high latitudes compared with the tropics. The mechanisms responsible for the similarity in the final response were not diagnosed. Later, Hansen et al. (1997) again looked at the radiative forcing of various phenomena, including ozone and aerosol heating, in addition to the two mentioned above. It was shown that the global-mean surface temperature response is approximately proportional to the global-mean radiative forcing (RF) at the tropopause. Therefore, the concept of RF at the tropopause became useful for the purpose of comparing global-mean surface response to various forcing, a concept later reinforced by the work of Joshi et al. (2003). Radiative forcing at the tropopause, adjusted after the stratosphere reaches radiative equilibrium, was adopted by the Intergovernmental Panel for Climate Change (IPCC) in its assessment reports (Forster 2007). It should be noted, however, that RF at the tropopause is a vertical integral of radiative heating at levels below, including that at the

Corresponding author address: Dr. K.-K. Tung, Department of Applied Mathematics, University of Washington, Seattle, WA 98195. E-mail: tung@amath.washington.edu

DOI: 10.1175/JAS-D-11-0117.1

surface. As a result, the RF representation of external forcing, depending on the type of forcing, could mask the large difference between troposphere and surface with regard to the meridional structure of radiative heating. For example, as shown in Hansen et al. (1997), the net downward radiative forcing at the surface due to the doubling of CO_2 has minimum at low latitudes and peak value at high latitudes. But as elevation increases, the latter shifts toward lower latitudes. At the tropopause level, its maximum is centered at the tropics. The net downward radiative forcing due to an increase in the solar constant, on the other hand, is largest in the tropics at all levels from the surface to the tropopause. So at the tropopause the two radiative forcings happen to have the same shape. The vertical and meridional structure of the external forcing in the entire troposphere, not just at the tropopause, contribute to determining the atmospheric dynamical response, which in turn contributes directly to the vertical and meridional structure of the (final) tropospheric and surface temperature changes. A more detailed diagnostics (than what is available in literature) of various vertical and horizontal transports of heat at different levels in the atmosphere and the radiative coupling of the atmosphere and surface will be presented here to show how these thermodynamic and dynamical processes lead to a similar response to 2% solar and $2 \times CO_2$ forcing.

The majority of existing methods for climate feedback analysis focus on quantifying the contribution to the global-mean climate sensitivity from radiative feedback processes (Bony et al. 2006, and references therein). Recently, a new method, called the coupled atmosphere–surface climate feedback–response analysis method (CFRAM), was formulated to explicitly separate contributions to the final (or total) temperature change and its spatial pattern due to the external forcing alone, and due to both radiative (local) and nonradiative feedback (local and nonlocal dynamic) processes (Lu and Cai 2009; Cai and Lu 2009). The three unique features of the CFRAM are (i) any changes in the energy cycle of the climate system, rather than just the radiative energy flux changes at the top of the atmosphere (TOA), are considered as climate feedbacks; (ii) the CFRAM enables us to calculate separately the partial temperature changes in response to the external forcing alone and to each of the subsequent radiative and nonradiative feedback processes as offline and postprocess diagnostic quantities without rerunning the original climate model, in contrast to the online-feedback suppression method (Hall and Manabe 1999; Schneider et al. 1999); and (iii) these partial temperature changes, by design, are additive and their sum can be directly compared with the total temperature change in response to the external forcing derived from the original climate simulation. In the present work, we will apply the CFRAM to diagnose the partial temperature changes due to the external forcing alone and also due to subsequent feedback processes.

2. Modeling experiments and climate feedback analysis method

We have made three sets of experiments with an aquaplanet coupled general circulation model, previously used by Lu and Cai (2010, hereafter LC2010). The simple coupled GCM consists of the National Aeronautics and Space Administration (NASA) Airborne Research Interferometer Evaluation System (ARIES)-Goddard Earth Observing System (GEOS) dry dynamical core (Suarez and Takacs 1995), a radiative transfer model (Fu and Liou 1992, 1993), a moist convective adjustment parameterization, a simple surface energy balance model without topography, and a simple boundary layer model that allows exchanges of sensible heat between atmosphere and surface. As in LC2010, the surface sensible heat flux is calculated by letting it be equal to the amount of energy required so that the vertical gradient of potential temperature in the atmospheric layer next to the ground is always equal to zero, corresponding a well-mixed boundary layer in the GCM. The surface albedo in the simple GCM is fixed and varies only with latitude, from 0.15 at the equator to 0.35 at the poles. The O_3 field in the simple GCM is fixed according to the zonal mean meridional and vertical profile of O_3 derived from the UK Universities Global Atmospheric Modelling Programme (UGAMP) ozone climatology (http://badc.nerc.ac.uk/view/badc.nerc.ac.uk__ATOM__dataent_UGAMPO3). There is no hydrological cycle in the simple GCM. However, this simple coupled GCM includes the water vapor feedback by fixing the model's relative humidity to a time-invariant meridional–vertical profile. The surface turbulent latent heat flux due to evaporation is substituted by surface turbulent sensible heat flux. The incoming solar forcing is a time invariant and zonally symmetric solar energy flux at the TOA, which is represented by the product of the solar constant and the annual mean meridional profile of the cosine of the solar zenith angle. All model parameter settings, including the meridional width of moist adiabatic lapse rate in the tropics, are identical to those reported in LC2010. The reader may consult LC2010 for more details about the model.

The first experiment is the control experiment (CNTL run), which is forced by the solar constant $S_0 = 1366$ W m^{-2} with the standard CO_2 concentration of 330 ppm. The second experiment is otherwise identical to the control experiment except that the standard CO_2 concentration is doubled to 660 ppm ($2CO_2$ run),

whereas the third experiment is the same as the control experiment except the solar constant is increased by 2%, to 1393.32 W m^{-2} (2%SOLAR run), corresponding to a uniform increase of solar irradiance by 2% at all wavelengths. Note that the global-mean radiative forcing at tropopause associated with a 2% increase in solar constant is roughly equivalent to that of a doubling of CO_2 (e.g., Hansen et al. 1984). All three experiments consist of 30 000 days of integrations and the outputs of the last 27 000 days of model integrations are used to obtain the time mean fields of each experiment. We have also performed 1% and 0.1% solar change experiments. These experiments are run much longer to achieve statistical significance when the signal to noise ratio is smaller. Because of the absence of zonal asymmetry in the external forcing and in the lower boundary, the longtime mean state of the coupled GCM is almost exactly zonally symmetric. Therefore, we only display the results as a function of latitude and/or height in all figures.

Throughout the paper, all (radiative and nonradiative) heating/cooling rates, or convergence/divergence of (radiative and nonradiative) energy fluxes, are defined in each sigma layer (not level) or surface layer on each horizontal grid in units of watts per square meter. The heating/cooling rates in units of watts per square meter in each layer on each grid point can be converted to the conventional units of kelvins per day by dividing a factor equaling to the product of the mass in the sigma layer (or surface layer) per unit area on the grid point and its heat capacity. The choice of the units of watts per square meter is solely for the sake of convenience in relating partial radiative cooling rate perturbation due to temperature change alone [i.e., $(\partial\mathbf{R}/\partial\mathbf{T})\Delta\mathbf{T}$ in (2)] to perturbations in convergence of various (radiative and nonradiative) energy fluxes without referring to (i) the vertical profile of atmospheric mass distribution and (ii) the differences in mass and heat capacity between the atmosphere and surface. In other words, we have treated each (atmospheric or surface) layer on each grid point as a ''volume object'' with a unit horizontal area (1 m^2) in writing the energy balance equation that involves energy transfers among neighbor volume objects via both radiative and nonradiative processes. By doing so, (radiative and nonradiative) energy fluxes ''entering'' or ''leaving'' an individual (atmospheric or surface) volume object through a particular surface of the volume object have the same units, namely watts per square meter, as the difference between ''incoming'' and ''outgoing'' energy fluxes. The difference between incoming and outgoing energy fluxes is defined as the convergence of energy fluxes into a volume object and the opposite difference is the divergence of energy fluxes out of a volume object (therefore, there is no need to take spatial derivatives in calculating energy convergence into or divergence out of a volume object).

We have applied the CFRAM to quantify contributions of external forcing and feedbacks to the temperature change pattern obtained from the 2%SOLAR and $2CO_2$ climate simulations. Specifically, at each latitude y, we first calculate the radiative heating/cooling rates listed in Table 1 in each atmospheric layer ($\sigma_{\text{top}} < \sigma < 1$, where $\sigma_{\text{top}} = 0.0005$ is the top level of the model in sigma coordinates) and at the surface layer ($\sigma = 1$) in units of watts per square meter using the radiative transfer model. From these radiative heating/cooling rates, we then calculate the following:

$$
\begin{aligned}
\Delta F^{\text{EXT\_2\%solar}}(y,\sigma) &= S^{2\%\text{solar}}(y,\sigma) - S^{\text{CNTL}}(y,\sigma),\\
\Delta F^{\text{EXT\_2CO}_2}(y,\sigma) &= S^{2\text{CO}_2}(y,\sigma) - R^{2\text{CO}_2}(y,\sigma) - [S^{\text{CNTL}}(y,\sigma) - R^{\text{CNTL}}(y,\sigma)],\\
\Delta F^{\text{WV\_2\%solar}}(y,\sigma) &= S^{\text{WV\_2\%solar}}(y,\sigma) - R^{\text{WV\_2\%solar}}(y,\sigma) - [S^{\text{CNTL}}(y,\sigma) - R^{\text{CNTL}}(y,\sigma)],\\
\Delta F^{\text{WV\_2CO}_2}(y,\sigma) &= S^{\text{WV\_2CO}_2}(y,\sigma) - R^{\text{WV\_2CO}_2}(y,\sigma) - [S^{\text{CNTL}}(y,\sigma) - R^{\text{CNTL}}(y,\sigma)]. \qquad (1)
\end{aligned}
$$

Throughout the paper, $S(y,\sigma)$ denotes the convergence of solar radiative energy flux at latitude y and layer σ ($\sigma = 1$ corresponds to the surface layer) whereas $R(y,\sigma)$ denotes the divergence of longwave radiative energy flux at latitude y and layer σ. Alternatively, we can also say that $S(y,\sigma)$ is the solar energy absorbed by the layer at (y,σ) per second whereas $R(y,\sigma)$ is equal to the difference between the longwave radiation energy emitted by the layer at (y,σ) per second and the longwave radiation absorbed by the layer at (y,σ) per second. It follows that the difference between S and R, or $S - R$, corresponds to the net radiative energy convergence at latitude y and layer σ. The vertical summation of $S - R$ from $\sigma = 1$ to $\sigma = \sigma_1$ corresponds to the net downward radiative flux at the level $\sigma = \sigma_1$. The term $S - R$, which has units of watts per square meter, can be converted to heating rate (K s^{-1}) by dividing by the product of the mass in the layer and its heat capacity.

Following LC2010, we also calculate two nonradiative heating perturbations in units of watts per square meter using the outputs of the 2%SOLAR and CNTL runs: one is $\Delta F^{\text{local\_dyn\_2\%solar}}(y,\sigma)$, changes in energy flux convergence due to convective energy transport, friction, and surface sensible heat flux, and the other is $\Delta F^{\text{lg\_dyn\_2\%solar}}(y,\sigma)$, changes in energy flux convergence

TABLE 1. Radiative heating/cooling rate calculations for the feedback analysis.

Convergence of shortwave radiation flux (W m^{-2})	Divergence of longwave radiation flux (W m^{-2})	Input fields
$S^{\mathrm{CNTL}}(y,\sigma)$	$R^{\mathrm{CNTL}}(y,\sigma)$	S_0 = 1366 W m^{-2}, CO_2 = 330 ppm, time mean fields of atmospheric water vapor and temperature of the CNTL run.
$S^{2\%\mathrm{solar}}(y,\sigma)$	—	As in CNTL, but S_0 = 1393.32 W m^{-2}.
$S^{2\mathrm{CO}_2}(y,\sigma)$	$R^{2\mathrm{CO}_2}(y,\sigma)$	As in CNTL, but CO_2 = 660 ppm.
$S^{\mathrm{WV\_2\%solar}}(y,\sigma)$	$R^{\mathrm{WV\_2\%solar}}(y,\sigma)$	As in CNTL, but using the time mean field of atmospheric water vapor derived from 2%SOLAR run.
$S^{\mathrm{WV\_2CO}_2}(y,\sigma)$	$R^{\mathrm{WV\_2CO}_2}(y,\sigma)$	As in CNTL, but using the time mean field of atmospheric water vapor derived from $2CO_2$ run.

due to large-scale energy transport. Similarly, we also obtain the two nonradiative heating perturbation terms from the outputs of the $2CO_2$ and CNTL runs: $\Delta F^{\mathrm{local\_dyn\_2CO}_2}(y,\sigma)$ and $\Delta F^{\mathrm{lg\_dyn\_2CO}_2}(y,\sigma)$.

Following the CFRAM formulation (Lu and Cai 2009; Cai and Lu 2009), we calculate a set of four partial temperature changes for the 2% SOLAR forcing and doubling of CO_2 cases using

$$\Delta\mathbf{T}^{\mathrm{EXT\_}X} = \left(\frac{\partial\mathbf{R}}{\partial\mathbf{T}}\right)^{-1}\Delta\mathbf{F}^{\mathrm{EXT\_}X}, \quad \Delta\mathbf{T}^{\mathrm{WV\_}X} = \left(\frac{\partial\mathbf{R}}{\partial\mathbf{T}}\right)^{-1}\Delta\mathbf{F}^{\mathrm{WV\_}X},$$
$$\Delta\mathbf{T}^{\mathrm{local\_dyn\_}X} = \left(\frac{\partial\mathbf{R}}{\partial\mathbf{T}}\right)^{-1}\Delta\mathbf{F}^{\mathrm{local\_dyn\_}X}, \quad \Delta\mathbf{T}^{\mathrm{lg\_dyn\_}X} = \left(\frac{\partial\mathbf{R}}{\partial\mathbf{T}}\right)^{-1}\Delta\mathbf{F}^{\mathrm{lg\_dyn\_}X}, \tag{2}$$

where X stands for either "2%solar" or "$2CO_2$" and $(\partial\mathbf{R}/\partial\mathbf{T})^{-1}$ is the inverse of the Planck feedback matrix $\partial\mathbf{R}/\partial\mathbf{T}$. The reader may consult Lu and Cai (2009) on the details of construction of the Planck feedback matrix using the time mean fields of the CNTL run. The four partial temperature changes, $\Delta\mathbf{T}^{\mathrm{EXT\_}X}$, $\Delta\mathbf{T}^{\mathrm{WV\_}X}$, $\Delta\mathbf{T}^{\mathrm{local\_dyn\_}X}$, and $\Delta\mathbf{T}^{\mathrm{lg\_dyn\_}X}$, correspond to temperature changes due to the external forcing alone and to water vapor feedback, local dynamical feedback (i.e., changes in convection, surface sensible heat flux, and in frictional processes), and large-scale dynamical feedback (i.e., changes in advective processes predicted by the dynamical core of the GCM), respectively. According to (2), each of these partial temperature changes is calculated by requiring the infrared radiation perturbation induced by the temperature change alone to exactly balance the energy flux convergence perturbation under consideration. We note that the vector symbols in (2) denote the vertical profiles of variables at a given horizontal location. Solving (2) latitude by latitude enables us to obtain the meridional (y) and vertical (σ) profiles of these partial temperature changes, which will be denoted without the vector symbol. The summations of these partial temperature changes are

$$\Delta T^{\mathrm{total\_}X} = \Delta T^{\mathrm{EXT\_}X} + \Delta T^{\mathrm{WV\_}X} + \Delta T^{\mathrm{local\_dyn\_}X} + \Delta T^{\mathrm{lg\_dyn\_}X}. \tag{3}$$

This will enable us to check the accuracy of these partial temperature calculations by comparing $\Delta T^{\mathrm{total\_2\%solar}}$ directly with $\Delta T^{2\%\mathrm{solar}}$ and $\Delta T^{\mathrm{total\_2CO}_2}$ with $\Delta T^{2\mathrm{CO}_2}$, where $\Delta T^{2\%\mathrm{solar}}$ and $\Delta T^{2\mathrm{CO}_2}$ are the time mean differences between 2%SOLAR and CNTL runs and between 2CO2 and CNTL runs, respectively.

3. Differences in external forcing and radiative equilibrium temperature

In the literature, external forcing typically is shown as the net downward radiative flux at a particular level (say tropopause or TOA). Hansen et al. (1997) in addition showed the net downward radiative flux perturbation of external forcing level by level. We define radiative heating (W m^{-2}) as the radiative flux convergence in each layer. The net downward radiative flux at a given level is obtainable from this radiative heating by integrating the latter at all layers below that level, including the surface. We plot in Fig. 1 the radiative heating perturbations of the external forcing in units of watts per square meter layer by layer in the atmosphere and at the surface. We have verified that the external forcings shown in Fig. 1 have spatial patterns similar to their counterparts shown in Hansen et al. (1997) after the conversion from radiative heating perturbations in layers to the perturbation in the net downward radiative flux at levels.

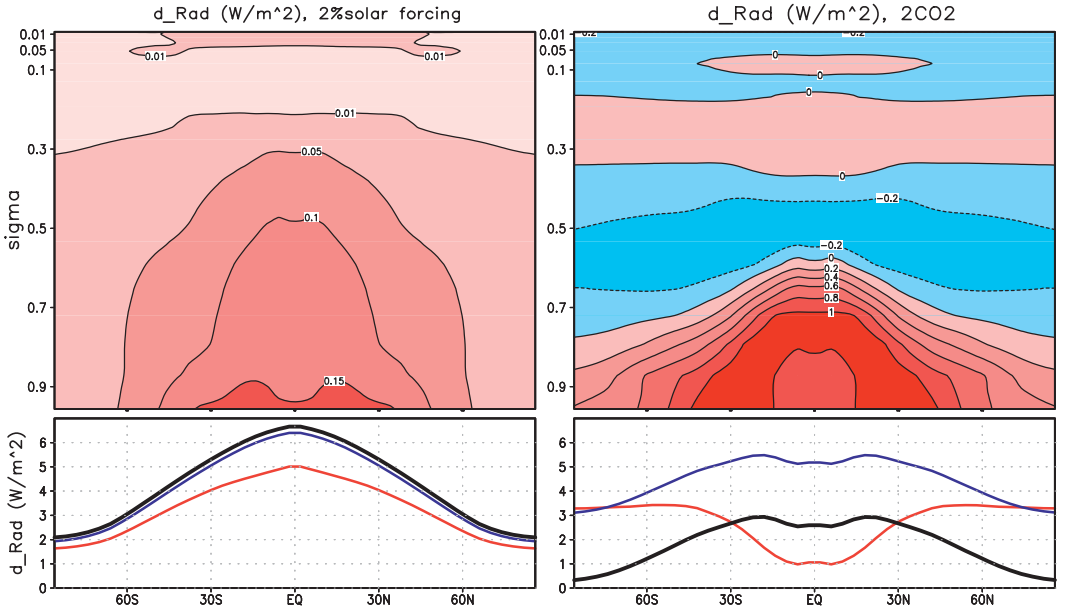

FIG. 1. Convergence of radiative energy flux perturbations due to external forcing. (left) $\Delta F^{\mathrm{EXT\_2\%solar}}$ (W m^{-2}) (top) in the atmosphere and (bottom) at the surface (red), at the tropopause (blue), and for the entire atmosphere and surface layer or the net external forcing at the top of the atmosphere (black). (right) $\Delta F^{\mathrm{EXT\_2CO_2}}$ (W m^{-2}) (top) in the atmosphere and (bottom) at the surface (red), at the tropopause (blue), and for the entire atmosphere and surface layer or the net external forcing at the top of the atmosphere (black).

Shown in the left panels of Fig. 1 are the radiative heating due to a 2% increase in solar constant in the atmosphere $\Delta F^{\mathrm{EXT\_2\%solar}}(y, \sigma < 1)$, and at the surface $\Delta F^{\mathrm{EXT\_2\%solar}}(y, \sigma = 1)$ (red curve in the bottom panel), for the 2% solar forcing case. It is seen that the radiative heating for the solar case is positive throughout the troposphere and stratosphere, as well as at the surface. The solar flux perturbation entering the atmosphere (black curve in Fig. 1b) peaks at the equator and decreases monotonically with latitude by a factor of about 3 at the poles. At the surface and throughout the atmosphere, the radiative heating for the solar forcing peaks at the equator and decreases with latitude, except for a thin layer near $\sigma = 0.1$ where radiative heating is slightly stronger in high latitudes (which is due to the decrease of the tropopause height with latitude).

The right panels of Fig. 1 show the radiative heating due to the doubling of CO_2 in the atmosphere, $\Delta F^{\mathrm{EXT\_2CO_2}}(y, \sigma < 1)$, and at the surface, $\Delta F^{\mathrm{EXT\_2CO_2}}(y, \sigma = 1)$ (the red curve in the bottom panel). The vertical summation of $\Delta F^{\mathrm{EXT\_2CO_2}}$ from $\sigma = 1$ to $\sigma = \sigma_{\mathrm{top}}$ corresponds to the net downward radiative forcing at the TOA due to the doubling of CO_2 (black curve in the bottom right panel). The radiative heating is negative throughout most part of the stratosphere (as indicated by $\Delta F^{\mathrm{EXT\_2CO_2}} < 0$ for $\sigma < 0.122$ in the top panel of Fig. 1 or by the difference between the black and blue curves in the bottom panel of Fig. 1). Its magnitude increases with height but weakly decreases with latitudes. At the surface, $\Delta F^{\mathrm{EXT\_2CO_2}}$ has minimum values (about 1 W m^{-2} at the equator) in the tropics and maximum values in high latitudes (about 3.3 W m^{-2} at the poles). In contrast to the surface layer, external radiative heating for the troposphere layer as a whole, as indicated by the difference between the blue and red curves in the bottom right panel in Fig. 1, is maximum in the tropics and decreases very rapidly with latitude, becoming negative at the poles. The maximum value of the external forcing in the tropical troposphere is about 4 times stronger than that at the surface below. The global-mean vertical structure of the external forcing obtained with our coupled GCM is similar to the results obtained from line-by-line radiation models and phase 3 of the Coupled Model Intercomparison Project (CMIP3)–IPCC Fourth Assessment Report (AR4) climate model simulations (Collins et al. 2006), showing the strongest heating at the surface, a smaller positive peak at 800 hPa, and then a general decreasing pattern at higher elevations. The general pattern shown in Fig. 1 is highly consistent with $\Delta F^{\mathrm{EXT\_2CO_2}}$ calculated using the outputs (including cloud fields) from the Geophysical Fluid Dynamics Laboratory (GFDL) CMIP3–IPCC AR4 and National Center for Atmospheric Research (NCAR) Community Climate System Model, version 4 (CCSM4) global warming climate simulations (not shown here).

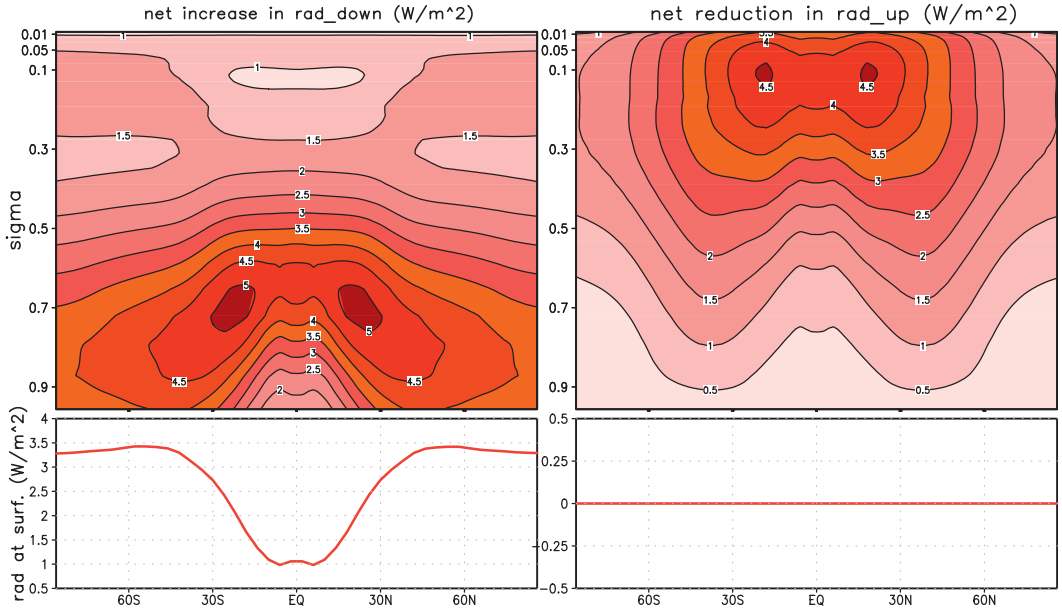

FIG. 2. Perturbations in (left) downward and (right) upward radiative energy fluxes (W m^{-2}) due to the doubling of CO_2 for (top) the atmosphere and (bottom) the surface.

Unlike $\Delta F^{\mathrm{EXT\_2\%solar}}$, which is mainly determined by the downward radiation flux perturbation, both downward and upward radiation flux perturbations contribute to the spatial pattern of $\Delta F^{\mathrm{EXT\_2CO_2}}$. Their combined effect is responsible for the relatively complicated spatial structure of $\Delta F^{\mathrm{EXT\_2CO_2}}$ shown in the right panels of Fig. 1, particularly the great disparity between the troposphere and surface. To highlight this, we show in Fig. 2 the net increase in downward radiation flux (left panels) and the net reduction in upward radiation flux (right panels) induced by the doubling of CO_2. As one may expect, $\Delta F^{\mathrm{EXT\_2CO_2}}$ at the surface is determined solely by the change in downward radiation. The layers below the axis of maximum values in the top left panel in Fig. 2 correspond to the place where absorption of the downward radiation emitted from the layers above takes place. The greater abundance of water vapor in the lower troposphere in the tropical time mean state results in a stronger absorption of downward radiation emitted from the upper troposphere, which is responsible for a minimum of the surface radiative forcing due to the doubling of CO_2 in the tropics. From the radiative transfer point of view, the consequence of a rapid decrease in atmospheric water vapor toward higher latitudes is the thinning of the atmospheric optical thickness. As a result, the level where the axis of maximum values of the downward radiation is located also descends with latitude. Over the polar region, the strongest absorption takes place at the surface, instead of in the lower troposphere, thereby causing maximum values of the surface radiative forcing there. The cold air temperature at the poles implies a weaker increase of the downward infrared radiation because the emission from the increased optical thickness due to the doubling of CO_2 is at cold air temperature in the polar region. As a result, the maximum external radiative forcing at the surface is found at latitudes away from the poles (where the atmospheric optical thickness is smallest in this model without clouds). The strong downward radiation emission from the middle to upper troposphere gives rise to a cooling perturbation in the layers above the axis of maximum values of the downward radiation fluxes.

The other direct effect of an increase in atmospheric CO_2 is a reduction in upward radiation flux at all levels (right panels of Fig. 2) except at the surface layer, where by definition longwave energy emission from the surface has to be the same without considering any feedbacks. The maximum reduction of upward radiation fluxes takes place at about 150 hPa, below which the reduction of upward radiation fluxes causes a heating perturbation and above which a cooling perturbation. The sum of the increase of downward radiation fluxes and the reduction of upward radiation fluxes corresponds to the profile of the increase in the net radiation heating due to the doubling of CO_2. The comparison between the left and right panels of Fig. 2 clearly indicates that the net downward radiation flux perturbation crossing the level 700 hPa is mainly caused by the increase in downward radiation fluxes emitted from the layers above, whereas

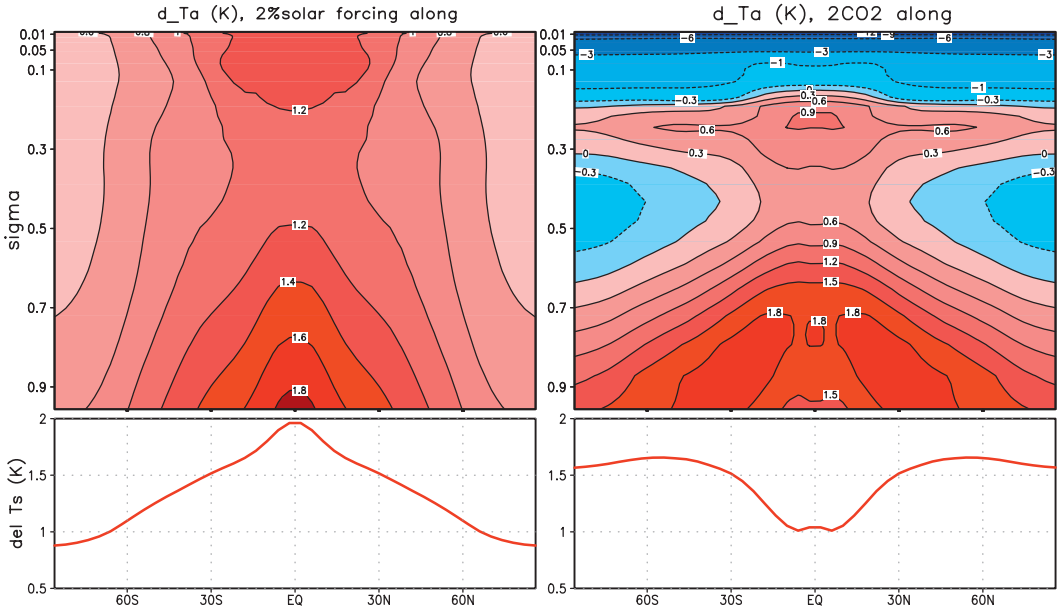

FIG. 3. Partial temperature changes due to external forcing alone: $\Delta T^{\mathrm{EXT\_2\%solar}}$ (top left) in the atmosphere and (bottom left) at the surface, and $\Delta T^{\mathrm{EXT\_2CO_2}}$ (top right) in the atmosphere and (bottom right) at the surface.

above 300 hPa it is mainly from the reduction of the upward radiation fluxes. It follows that there exists a minimum value of the net downward radiation flux perturbation between 700 and 300 hPa. In the layers below the minimum value level and above the maximum value (i.e., 700 hPa) lies the cooling perturbation due to the external forcing. This explains the band structure of $\Delta F^{\mathrm{EXT\_2CO_2}}$ in the vertical as shown in the top right panel of Fig. 1.

The different radiative forcing is responsible for the very different radiative equilibrium temperature response, also called the direct temperature response, which is calculated directly from the external forcing without taking into account of feedback processes. The spatial variation of the direct temperature response to external solar forcing exhibits a meridionally decreasing warming pattern from the equator to the poles in the entire atmosphere and at the surface (Fig. 3, left panels). Vertically, the warming decreases with height from the surface to the tropopause and then increases with height above the tropopause. The surface warming is maximum at the equator (about 1.95 K) and minimum at the poles (about 0.9 K). The spatial pattern of the direct temperature response to greenhouse gas heating is distinctly different from that of solar (Fig. 3, right panels). The direct greenhouse heating response in temperature has a vertically increasing cooling pattern in the stratosphere. The cooling in the stratosphere is slightly stronger in the poles than that at the equator. Note that $\Delta T^{\mathrm{EXT\_2CO_2}}$ displays a general warming pattern throughout the troposphere except in the midtroposphere in high latitudes where temperature decreases in response to the cooling imposed by $\Delta F^{\mathrm{EXT\_2CO_2}}$. At the surface, the direct warming due to greenhouse heating is stronger at high latitudes than at low latitudes, whereas in the troposphere the tropical warming due to the external forcing is stronger than at high latitudes.

4. Similarity in the total response

Despite the drastic contrast between the radiative heating and hence equilibrium temperature responses, the total temperature response to solar forcing (left panels of Fig. 4) is quite similar to that for greenhouse gas heating (right panels of Fig. 4) in the troposphere and at the surface. From the middle to upper troposphere both total temperature responses show maximum warming in the tropics and minimum warming at high latitudes. At the surface, the minimum temperature response is found at the equator in contrast to the situation aloft, warmed by about 1.7 K in both the solar and the greenhouse gas cases. This is quite remarkable since the radiative equilibrium responses at the surface are a factor of 2 different at the equator for the two cases. Higher final temperature response is found outside the tropics, reaching about 3 K in both forcing cases. There is a local maximum in temperature at the edge of the tropics, at around 30° in both the solar and greenhouse cases. The phenomenon of polar amplification of

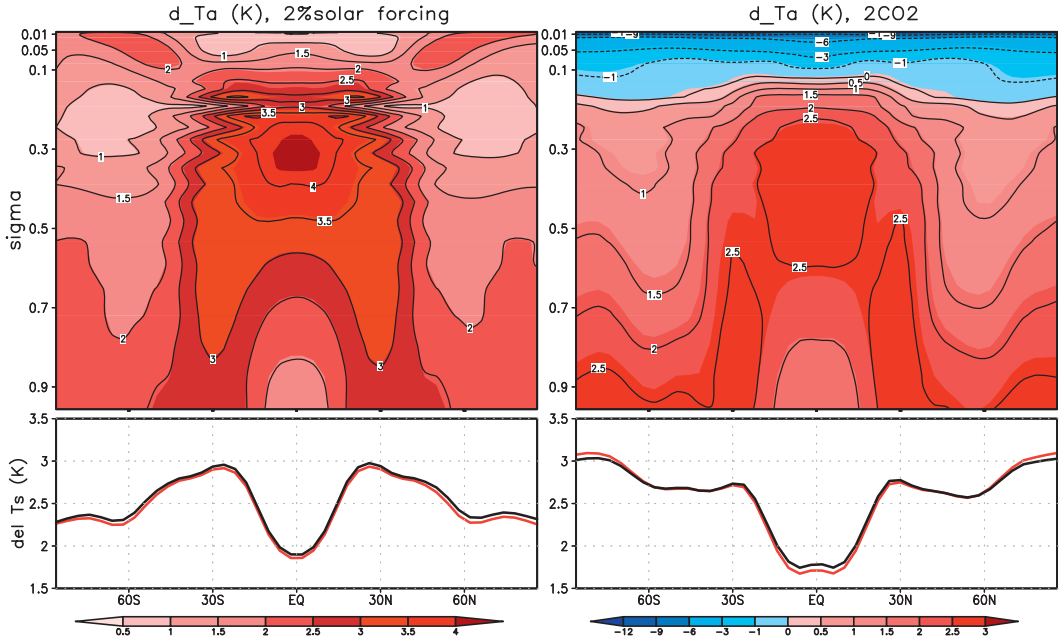

FIG. 4. Changes in (top) atmospheric temperature and (bottom) surface temperature. Shading and red curve are derived from the time mean differences of (left) the 102% and 100% solar forcing climate simulations and (right) the $2 \times CO_2$ and $1 \times CO_2$ climate simulations. Contours and the black curve are obtained from the sum of the partial temperature changes displayed in the corresponding panels in Figs. 3, 6, 8, and 10.

warming is present in both cases, in the sense that polar warming is stronger than equatorial warming. However, in the solar case, the polar warming is lower than in the subtropics, whereas in the greenhouse case the warming maximum takes place at the poles. Our model does not have ice–albedo feedback. It is expected that ice–albedo feedback would increase the polar warming, resulting in a polar maximum in response in the solar case as in the greenhouse case. Another important common feature in the two cases is that in the tropics, the warming is stronger in the upper troposphere than in the lower troposphere and at the surface, whereas at high latitudes the strongest warming occurs at surface.

In the stratosphere, the dramatic difference between $\Delta T^{2\%solar}$ and ΔT^{2CO_2} can be traced to the difference between $\Delta T^{EXT\_2\%solar}$ and $\Delta T^{EXT\_2CO_2}$, unlike that in troposphere. However, in terms of spatial gradient, the total response to the solar forcing and to greenhouse forcing is quite similar. Specifically, in the tropical stratosphere, both $\Delta T^{2\%solar}$ and ΔT^{2CO_2} show a reduction of the vertical temperature gradient. Moreover, the meridional temperature gradient in the stratosphere is also reduced from subtropics to pole in both cases, as evident from the maximum warming for the solar forcing case and the minimum cooling for the greenhouse forcing case in the polar upper stratosphere. These two common features are particularly remarkable since both $\Delta T^{EXT\_2\%solar}$ and $\Delta T^{EXT\_2CO_2}$ reach minimum in high latitudes and $\Delta T^{EXT\_2\%solar}$ increase with height in the stratosphere.

5. Contributions to the temperature response from feedbacks

To understand why the response at the surface and in the troposphere is so similar when the forcing is so different for the two forcing cases, we need to diagnose the various feedbacks that add to the radiative equilibrium response. The feedbacks included in the idealized GCM model are (i) water vapor feedback, (ii) surface sensible flux feedback and vertical convection feedback, and (iii) large-scale dynamical feedback. As indicated in (2) and (3), we have obtained $\Delta T^{WV\_2\%solar}$, $\Delta T^{local\_dyn\_2\%solar}$, and $\Delta T^{lg\_dyn\_2\%solar}$ for the solar forcing case, and $\Delta T^{WV\_2CO_2}$, $\Delta T^{local\_dyn\_2CO_2}$, and $\Delta T^{lg\_dyn\_2CO_2}$ for the greenhouse forcing case, where the terms with superscript ''WV'' are the partial temperature changes due to water vapor feedback, those with superscript ''local_dyn'' are the partial temperature changes due to surface sensible feedback and vertical convection feedback (also including the change in the frictional force, which is a smaller term), and those with superscript ''lg_dyn'' are the partial temperature changes due to large-scale dynamical feedback. Together with the partial temperature changes due to external forcing alone (the radiative equilibrium temperature) shown in Fig. 3, we have

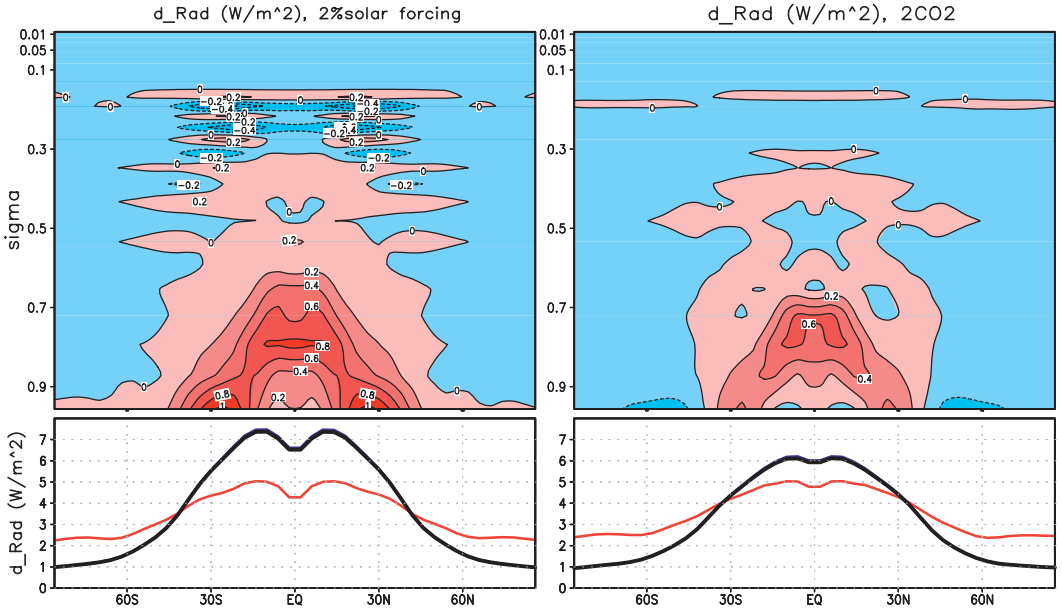

FIG. 5. As in Fig. 1, but for radiative energy perturbations due to water vapor feedback.

obtained four partial temperature changes for each type of external forcing. The accuracy of these partial temperature change calculations can be checked by comparing the sum of these partial temperature changes (contours in top panels of Fig. 4 and black curve in bottom panels of Fig. 4) with the total temperature change derived from the original GCM climate simulations (shading in the top panels and red curve in the bottom panels in Fig. 4). It is seen that the sum of these partial temperature changes is very close to the temperature change obtained directly from the climate simulations. This confirms that these partial temperature changes due to the external forcing and feedbacks indeed add up to the total temperature change obtained from the original model.

The change in atmospheric specific humidity in our simple model follows the temperature change because of the fixed relative humidity assumption in the model. When the relative humidity is kept constant, changes in atmospheric water vapor in response to the external forcing are more related to the climatological mean temperature profile in the control run through the Clausius–Clapeyron relation than to the temperature change itself. As a result, the increase in atmospheric specific humidity in both cases shows a maximum in the tropical lower troposphere and decreases with latitude and height rapidly (not shown here).

The greater amount of water vapor increase in the tropics results in maximum values of $\Delta F^{\mathrm{WV\_2\%solar}}$ and $\Delta F^{\mathrm{WV\_2CO_2}}$ in the tropical area. As the CO_2-induced radiative forcing (Fig. 1), the radiative heating due to change in water vapor also has maximum values at the surface (the red curve in the bottom panels of Fig. 4; the differences between black and red curves corresponds to the net radiative energy flux perturbations in the atmospheric column). The change in water vapor alone causes a reduction of the net radiative energy flux convergence at high-latitude atmosphere (Fig. 5, top panels). The positive values of $\Delta F^{\mathrm{WV\_2\%solar}}$ and $\Delta F^{\mathrm{WV\_2CO_2}}$ are mainly found in the tropics and subtropics. It follows that the water vapor feedback acts to put more energy perturbation at low latitudes than at high latitudes. The heating at the surface and cooling in the atmosphere (or in the upper atmosphere in the tropics) due to water vapor feedback obtained with our simple coupled GCM is consistent with the results from more sophisticated GCMs (Mitchell et al. 1987), line-by-line radiation models, and CMIP3–IPCC AR4 climate simulations (Collins et al. 2006).

The temperature change due to water vapor feedback exhibits a very similar meridional and vertical profile for both solar forcing and greenhouse cases, other than that $\Delta T^{\mathrm{WV\_2\%solar}}$ is larger than $\Delta T^{\mathrm{WV\_2CO_2}}$ because of a larger increase in water vapor for the solar forcing case (Fig. 6). This can be explained by the fact that the change in water vapor is temperature dependent in our idealized GCM and the change in total temperature is quite similar in both forcing cases in the tropical troposphere. The increase in atmospheric specific humidity mainly takes place in the tropical troposphere and it decreases with latitude and height rapidly (not shown). Such a meridional profile of water vapor change results

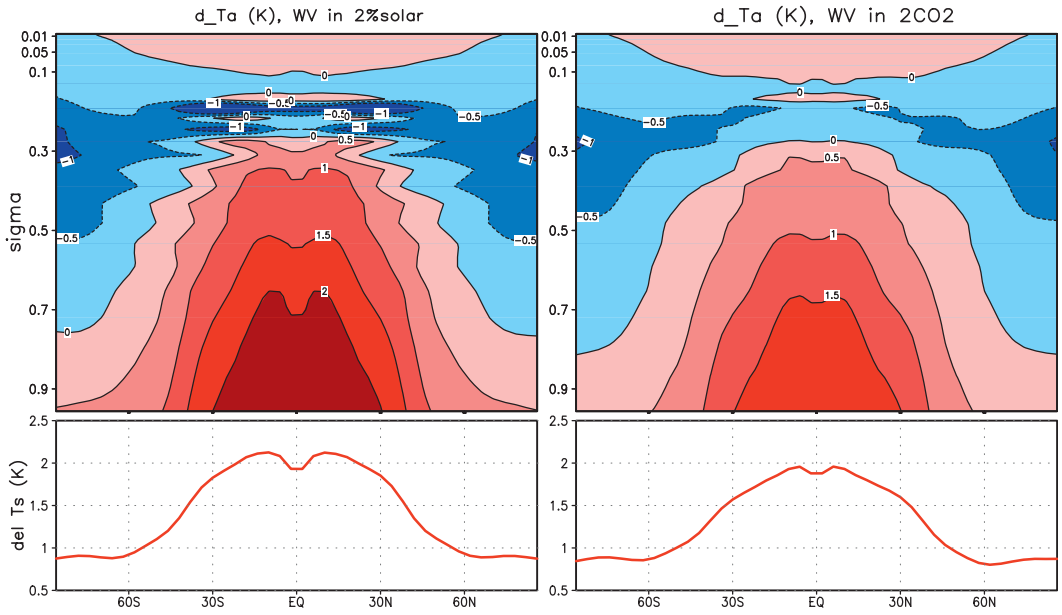

FIG. 6. As in Fig. 3, but for (left) $\Delta T^{\mathrm{WV\_2\%solar}}$ and (right) $\Delta T^{\mathrm{WV\_2CO_2}}$.

in stronger water vapor feedback in the tropics and weaker water vapor feedback in high latitudes. The extra surface warming in the tropics due to water vapor feedback is about twice as large as that in high latitudes. Water vapor feedback also leads to warming in the lower half of the troposphere. The vertical extent of the warming in the lower half of the troposphere due to water vapor feedback is deep, up to 300 hPa, and it decreases with latitude very rapidly. Water vapor feedback causes cooling in the upper troposphere. Both intensity and vertical extent of the cooling in the upper troposphere due to water vapor feedback are maximum at high latitudes. The vertical profile of temperature change in the tropical troposphere due to water vapor feedback resembles that due to the doubling of CO_2 forcing, showing two pairs of positive–negative pattern from the surface to tropopause. In our model experiments, we use a constant specific humidity equal to 0.002 g kg^{-1} for the stratosphere ($\sigma < 0.14$), responsible for very small values of $\Delta T^{\mathrm{WV\_2\%solar}}$ and $\Delta T^{\mathrm{WV\_2CO_2}}$ in the stratosphere.

The nonradiative energy perturbations due to changes in surface sensible heat flux (representing ''evaporation'' feedback in this GCM model without an interactive hydrological cycle) and convection (local dynamic feedbacks) for both types of external forcing are shown in Fig. 7. Note that the vertical summation of energy perturbations due to local dynamic feedbacks is zero. In both cases, the local dynamic feedbacks are mainly confined in the tropics, showing maximum cooling at the surface and lower troposphere and maximum heating in upper troposphere, consistent with the effects of vertical convection. Shown in Fig. 8 are $\Delta T^{\mathrm{local\_dyn\_2\%solar}}$ and $\Delta T^{\mathrm{local\_dyn\_2CO_2}}$, partial temperature changes in response to nonradiative energy perturbations $\Delta F^{\mathrm{local\_dyn\_2\%solar}}$ and $\Delta F^{\mathrm{local\_dyn\_2CO_2}}$, respectively. Enhancement of surface turbulent flux and vertical convection in the tropics in response to external forcing causes a warming reduction at the surface, a negative feedback, while it amplifies warming in upper troposphere in the tropics, a positive feedback. In response to a stronger enhancement of surface turbulent flux and vertical convection in the tropics for the solar forcing case, the dynamical warming reduction at the surface and in lower troposphere and warming amplification in upper troposphere in the tropics are much stronger than those for the greenhouse gas forcing case. Outside of the tropics in the troposphere and in the stratosphere, there is little temperature change due to surface turbulent flux and vertical convection feedback.

The intensification of the atmospheric meridional temperature gradient, particularly in the upper troposphere, as a result of the combined effect of the external forcing (Fig. 2, top panels), water vapor feedback (Fig. 6, top panels), and convective feedback (Fig. 8, top panels) for both forcing cases, drives a stronger large-scale poleward energy transport in the mid- and upper troposphere (Fig. 9). The spatial patterns of large-scale dynamical feedback for the solar and CO_2 cases are remarkably similar. The vertical summation of the energy perturbations due to large-scale dynamic feedbacks (black curves in the bottom panels of Fig. 9) shows

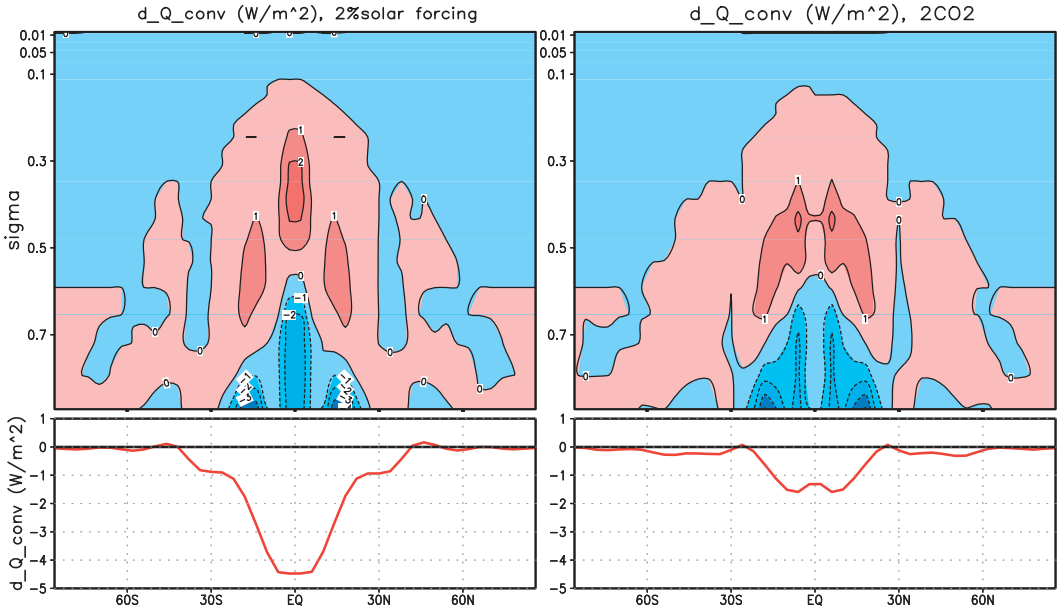

FIG. 7. (top) Nonradiative energy perturbations due to local dynamical (convective and friction) feedbacks. (bottom) The red curves are energy perturbations due to convective feedbacks at the surface and the black lines correspond to the vertical sum of energy perturbations due to convective feedbacks over all atmospheric layers and the surface layer, which are exactly equal to zero.

positive values at high latitudes and negative values at low latitudes, indicating a strengthening of poleward energy transport in both cases. The intensity of the enhancement of poleward energy transport is stronger in the solar forcing case. The strengthening of poleward energy transport results in the enhancement of both the surplus in low latitudes and deficit in high latitudes of the net radiation flux at the TOA (blue curves in the bottom panels of Fig. 9). The enhancement of the poleward dynamical energy transport causes additional warming in high latitudes at the expense of low latitudes in both stratosphere and troposphere (Fig. 10, top panels). Note

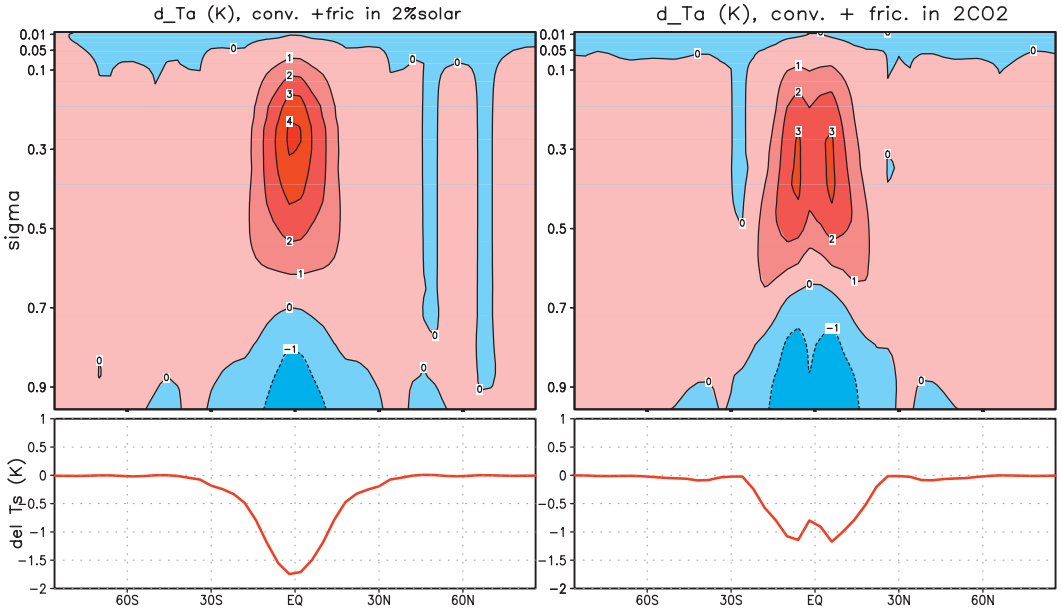

FIG. 8. As in Fig. 3, but for (left) $\Delta T^{\text{loc\_dyn\_2\%solar}}$ and (right) $\Delta T^{\text{loc\_dyn\_2CO}_2}$.

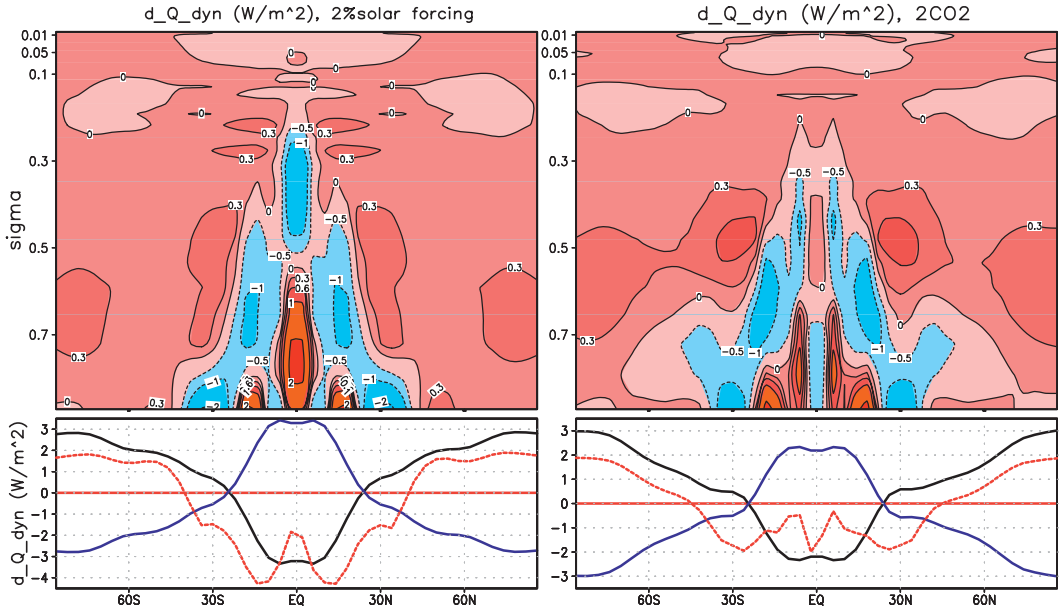

FIG. 9. As in Fig. 7, but for (top) nonradiative energy perturbations due to nonlocal large-scale dynamical feedbacks. (bottom) The red lines in bottom panels are energy perturbations due to large-scale feedback at the surface, which by definition is zero since there is no horizontal energy transport at the surface in our simple coupled GCM model. The black curves correspond to the vertical sum of energy perturbations due to large-scale dynamical feedbacks over all atmospheric layers, whereas the blue curves are the changes in the net radiative energy fluxes at the TOA. The black curve is almost exactly the same as the negative of the blue curve. The global mean of either the black or blue curve is (almost) exactly zero. The dotted red curves correspond to the numerator of (4), representing changes in downward longwave radiation at the surface emitted from the atmosphere due to atmospheric large-scale dynamics induced air temperature changes.

that there is no large-scale horizontal energy transport at the surface in our coupled GCM model (which does not have a dynamically active ocean). However, the enhanced atmospheric poleward energy transport aloft can still cause surface warming amplification in high latitudes by enhancing downward infrared radiation from a warmed polar troposphere, and warming reduction in low latitudes by reducing downward infrared radiation (Cai 2005, 2006). This can be illustrated from the analytical expression for the surface temperature change due to the enhancement in atmospheric poleward energy transport $\Delta T_s^{\text{lg\_dyn\_X}}$ (the curves in the bottom panels of Fig. 10), which is

$$\Delta T_s^{\text{lg\_dyn\_X}} = \frac{-\left[\sum_{\text{all atmospheric layers } j} (\partial R_S/\partial T_j)\Delta T_j^{\text{lg\_dyn\_X}}\right]}{\partial R_S/\partial T_S}, \tag{4}$$

where $\partial R_S/\partial T_j$ is the downward longwave radiation flux perturbation at the surface due to one unit change of air temperature at the jth layer, and $\partial R_S/\partial T_S$ is the upward longwave radiation flux perturbation at the surface due to one unit change of surface temperature. The term in the numerator of (4) corresponds to the total downward longwave radiation flux perturbation at the surface due to atmospheric large-scale dynamics induced air temperature changes.

The numerator in (4) is displayed as the dotted red curves in the bottom panels of Fig. 9. It is seen that there is a reduction of 2–4 W m^{-2} in the downward longwave radiation in low latitudes due to cooler temperature anomaly induced by the enhanced atmospheric poleward energy transport. In high latitudes, the air temperature warming induced by the enhanced atmospheric poleward energy transport is attributable to an enhancement of up to 2 W m^{-2} in the downward longwave radiation to the surface. According to (4), $\Delta T_s^{\text{lg\_dyn\_X}}$ is determined in such a way that the corresponding change in the upward longwave radiation emitted from the surface is exactly (in the linear sense) balanced by the atmospheric large-scale dynamics–induced downward longwave radiation perturbation. As indicated in the bottom panels of Fig. 10, $\Delta T_s^{\text{lg\_dyn\_X}}$ is positive in high latitudes to balance the enhancement in the downward longwave radiation from a dynamics-induced warmer polar troposphere and is negative in low latitudes to balance the reduction in the downward longwave

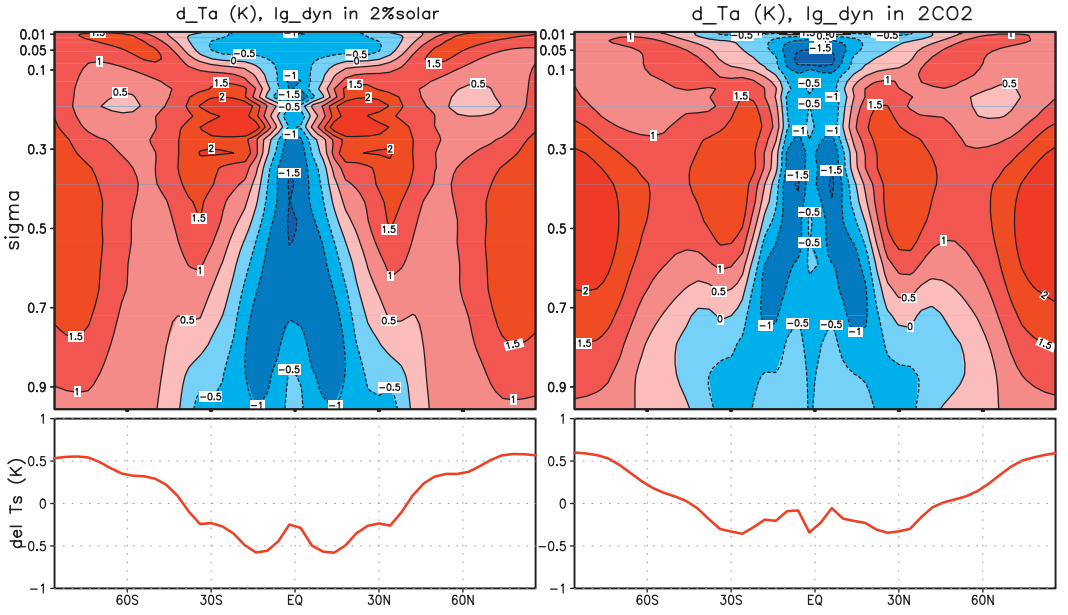

FIG. 10. As in Fig. 3, but for (left) $\Delta T^{\text{lg\_dyn\_2\%solar}}$ and (right) $\Delta T^{\text{lg\_dyn\_2CO}_2}$.

radiation from a dynamics-induced cooler tropical troposphere.

6. How useful is RF at the tropopause?

As indicated in Fig. 1, most of the radiative forcing due to an increase in solar constant at the tropopause level passes through to the surface because it is of short wavelength and so there is little difference at the two levels. For the 2 × CO_2 case, most of the RF in the tropopause in the tropics is applied at the lower troposphere instead of at the surface whereas in high latitudes there is little difference between the RF at the tropopause and surface. As a result, the RF at the tropopause for the 2 × CO_2 case has the opposite meridional profile from that at the surface. At the tropopause, the RF for the 2% solar forcing case is similar to that for the 2 × CO_2 case (see the blue curve in Fig. 1). For two forcings that have the same RF at the tropopause, the vertical integrated radiative heating for the vertical troposphere column (including the surface) is the same. We therefore expect the columnar radiative equilibrium response to be the same and exhibit the same meridional structure as the RF at the tropopause. This is indeed the case, as shown in Fig. 11.

Following Jiang and Deng (2011) and Deng et al. (2012), we define the vertical pattern-amplitude projection (VPAP$^{(i)}$), measuring the contributions to the total temperature change in the troposphere–surface column from $\Delta T^{(i)}$ ($\Delta T^{(i)}$ is one of the partial temperature changes determined from CFRAM analysis) according to

$$\text{VPAP}^{(i)} = \frac{\dfrac{1}{p_s - p_t}\displaystyle\int_{p_t}^{p_s} \Delta T^{(i)} \Delta T \, dp}{\sqrt{\dfrac{1}{p_s - p_t}\displaystyle\int_{p_t}^{p_s} \Delta T^2 \, dp}}, \tag{5}$$

where p_s is the surface pressure and p_t = 191 hPa, representing the level below which the total temperature change in both cases is positive everywhere. Because the sum of all $\Delta T^{(i)}$ converges to ΔT as indicated in Fig. 3, we have that the sum of all of VPAP$^{(i)}$ converges to the mass weighted root-mean-square amplitude of the total temperature change in the tropopause–surface column (in the level below 191 hPa), equaling $\sqrt{[1/(p_s - p_t)]\int_{p_t}^{p_s} \Delta T^2 \, dp}$. Because below p_t = 191 hPa ΔT is always positive in both cases, we define the mass weighted mean temperature change in the troposphere–surface column as $\sqrt{[1/(p_s - p_t)]\int_{p_t}^{p_s} \Delta T^2 \, dp}$, which corresponds to the black curve in Fig. 11. It is seen that other than the small difference in magnitude, which merely reflects the fact that amplitude of the 2% solar forcing is slightly stronger than the 2 × CO_2 forcing, there is little difference in the warming pattern of the troposphere–surface column between the two cases. The direct mean response in the troposphere–surface column follows the RF at the tropopause very closely, showing a poleward decreasing meridional pattern in both cases (beige bars in Fig. 11). Water vapor feedback and convection are active mostly in the tropics. These two feedback processes warm the tropics and sharpen the negative meridional gradients. On top of these the large-scale

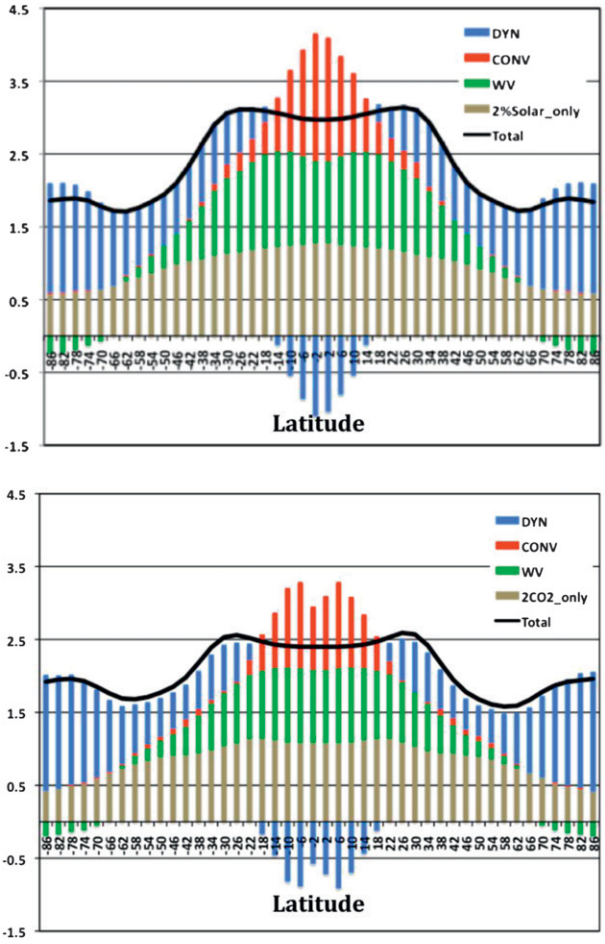

FIG. 11. Contributions to the change of the troposphere–surface (from the surface to 191.8 hPa) mean temperature (K) from the external forcing alone, and from water vapor, convective, and large-scale dynamical feedbacks as a function of latitude (abscissa), for (top) the 2% solar forcing case and (bottom) the 2 × CO_2 case. The sum of all color bars at each latitude is equal to the black curve, which is the (total) change of the troposphere–surface mean temperature.

dynamical processes act to transport heat from the tropics to the high latitudes. This transport is very similar in the two forcing cases. It is not surprising that in the end the final columnar response is very similar in the two forcing cases. So it appears that for two forcing cases, if their RF at the tropopause is similar, their final column-mean temperature response should be similar, although the final response is very different in shape from that of the RF for each forcing. Note also that the similarity of the final responses of the two forcing cases is much greater than the similarity of their RFs at the tropopause. The results shown in Fig. 11 indicate that large-scale dynamical nonradiative feedback processes play an important and flexible role in shaping the final response to the external forcing.

7. Changes in atmospheric circulation

The similarity in large-scale poleward energy transport should be accompanied by a similarity in the change of atmospheric circulation. Indeed, the change in the zonal mean zonal wind for the two cases is remarkably similar. The common features between the top panels in Fig. 12 are (i) poleward shifting of subtropical jets in both hemispheres, (ii) intensification of westerlies in midlatitudes, (iii) poleward expansion of the subtropical easterlies, (iv) intensification of polar easterlies, and (v) reduction of easterlies in the equatorial belt. The great similarity in the change of circulation between the solar forcing and greenhouse gas forcing case is also reflected in surface pressure (Fig. 12, bottom panels). Both types of forcing result in a rise of surface pressure in low latitudes and a decrease in high latitudes. The increase of surface pressure is strongest along 34° of latitude whereas the decrease of surface pressure is strongest along 58° of latitude. The locations of the maximum positive and negative surface pressure changes are 8°–12° poleward of the maximum (26° of latitude) and minimum (46° of latitude) surface pressure in the (unperturbed) time mean state (the black line in the bottom panels of Fig. 12). Both intensification and a poleward shift of the mean meridional surface pressure gradient pattern are displayed, as well as the associated surface wind pattern.

8. Summary

In this paper, we compare the climate response to 2% solar and 2 × CO_2 forcing and provide a quantitative analysis on how various radiative and nonradiative feedback processes redistribute energy spatially (both vertically and horizontally) in such a way that the final response to the two types of forcing is quite similar despite the differences in the spatial patterns of the two types of external forcing. Previously radiative forcing (RF) at the tropopause has been commonly used to characterize climate forcing. While useful for the vertical column, it masks differences in forcing at the surface and troposphere. On an annual mean basis, the solar heating at the surface peaks at the equator and has minimum values in the poles, where greenhouse heating actually attains a minimum at the equator and maximum values in high latitudes. In the atmosphere, the heating perturbation due to 2% solar constant increase is positive everywhere, with the peak values in low troposphere and stratosphere in the tropics. The heating due to the doubling of CO_2, however, is negative in most parts of the atmosphere except in the lower troposphere in the tropics where the positive maximum center is

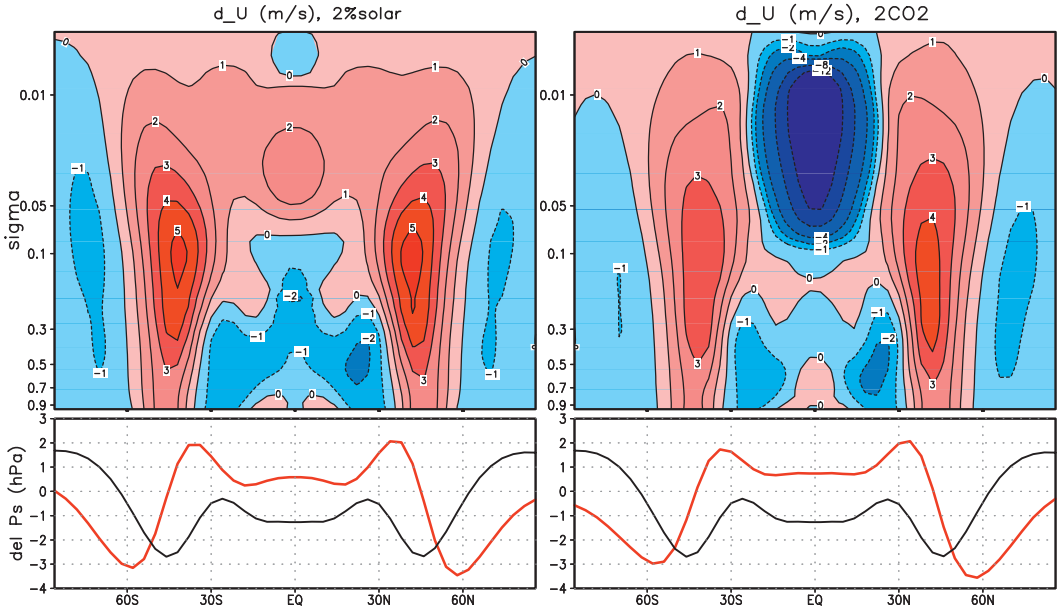

FIG. 12. Changes in (top) zonal mean zonal wind (m s^{-1}) and (bottom) surface pressure (hPa) due to (left) 2% solar forcing and (right) doubling of CO_2. In the bottom panels the red line represents changes in surface pressure, and the black line is $(P_s - 1005)/5$, where P_s is the climatological surface pressure of the control experiment.

located. As a result the radiative equilibrium temperature is very different for the two cases. Nevertheless, these two types of external forcing have two common features in the troposphere in terms of spatial gradient: they both decrease with height strongly from the lower troposphere to the upper troposphere in the tropics and they both decrease with latitude strongly in the troposphere. The radiative energy flux perturbation due to water vapor feedback further enhances the vertical gradient of radiative forcing in the tropics and the meridional gradient in the lower troposphere. In response to the vertically decreasing radiative energy perturbation in the tropics, the surface turbulent heat flux feedback and convective feedback act to reduce the warming at the surface and in the lower troposphere while amplifying it in the upper troposphere. It follows that all the factors, including the external forcing, water vapor feedback, and enhancement of convection in the tropics act collectively, causing a poleward-decreasing profile of energy flux convergence perturbations throughout the troposphere. In response to the meridionally decreasing energy perturbations, large-scale dynamical feedback acts to transport more heat to the high latitudes and is responsible for a warming amplification at high-latitude atmosphere. The additional warming of the atmosphere at high latitudes gives rises to a stronger downward infrared radiation to the surface below, causing a surface warming amplification at high latitudes. The similarity in large-scale poleward energy transport leads to a remarkable similarity in the change of atmospheric circulation, including poleward shifting of subtropical jets and stratospheric polar jets, poleward expansion of the subtropical easterlies, and intensification of polar easterlies. Furthermore, both types of forcing result in a rise of surface pressure at low latitudes and a decrease at high latitudes. There are both intensification and poleward shift of the mean meridional surface pressure gradient pattern, as well as the associated surface wind pattern.

The two forcing experiments are hypothetical and are not intended as simulations for global warming due to greenhouse gases or for the 11-yr solar cycle problem. A proper simulation of these two phenomena requires time-dependent calculations using a coupled atmosphere–ocean GCM. Nevertheless, the mechanisms that we discuss here—the convective feedback, the water vapor feedback, and large-scale dynamical transports—all occur at short time scales, from hours to months. Therefore we expect the results discussed here to be of relevance to the two real physical phenomena, although in the case of 11-yr solar cycle there is an additional thermal heating due to ozone in the stratosphere that we have not considered in detail. Two deficiencies here include the fact that ozone is fixed when we know that ultraviolet radiation produces more ozone in the stratosphere, and the fact that currently the portion of the solar radiation that is in the ultraviolet range is uncertain.

Acknowledgments. The authors are grateful for the constructive comments from the editor Dr. R. Garcia and the anonymous reviewers. MC was supported by grants from Chinese Ministry of Science and Technology (2010CB951600), National Science Foundation (ATM-0833001), Department of Energy (DE-SC0004974), and the NOAA CPO/CPPA program (NA10OAR4310168) KKT is supported by National Science Foundation, Climate Dynamics Program through Grants ATM 0808375 and DMS 0940342, and National Aeronautical and Space Administration, under Grant NNX11AC75G.

REFERENCES

Bony, S., and Coauthors, 2006: How well do we understand and evaluate climate change feedback processes? *J. Climate,* **19,** 3445–3482.

Cai, M., 2005: Dynamical amplification of polar warming. *Geophys. Res. Lett.,* **32,** L22710, doi:10.1029/2005GL024481.

——, 2006: Dynamical greenhouse-plus feedback and polar warming amplification. Part I: A dry radiative-transportive climate model. *Climate Dyn.,* **26,** 661–675.

——, and J.-H. Lu, 2009: A new framework for isolating individual feedback processes in coupled general circulation climate models. Part II: Method demonstrations and comparisons. *Climate Dyn.,* **32,** 887–900, doi:10.1007/s00382-008-0424-4.

Collins, W. D., and Coauthors, 2006: Radiative forcing by well-mixed greenhouse gases: Estimates from climate models in the IPCC AR4. *J. Geophys. Res.,* **111,** D14317, doi:10.1029/2005JD006713.

Deng, Y., T.-K. Park, and M. Cai, 2012: Process-based decomposition of the global surface temperature response to El Niño in boreal winter. *J. Atmos. Sci.,* **69,** 1706–1712.

Forster, P., and Coauthors, 2007: Changes in atmospheric constituents and in radiative forcing. *Climate Change 2007: The Physical Science Basis,* S. Solomon et al., Eds., Cambridge University Press, 129–234.

Fu, Q., and K. N. Liou, 1992: On the correlated *k*-distribution method for radiative transfer in nonhomogeneous atmosphere. *J. Atmos. Sci.,* **49,** 2139–2156.

——, and ——, 1993: Parameterization of the radiative properties of cirrus clouds. *J. Atmos. Sci.,* **50,** 2008–2025.

Hall, A., and S. Manabe, 1999: The role of water vapour feedback in unperturbed climate variability and global warming. *J. Climate,* **12,** 2327–2346.

Hansen, J., and Coauthors, 1984: Climate sensitivity: Analysis of feedback mechanisms. *Climate Processes and Climate Sensitivity, Geophys. Monogr.,* Vol. 29, Amer. Geophys. Union, 130–163.

——, M. Sato, and R. Ruedy, 1997: Radiative forcing and climate response. *J. Geophys. Res.,* **102,** 6831–6864.

Jiang, T., and Y. Deng, 2011: Downstream modulation of North Pacific atmospheric river activity by East Asian cold surges. *Geophys. Res. Lett.,* **38,** L20807, doi:10.1029/2011GL049462.

Joshi, M., K. Shine, M. Ponater, N. Stuber, R. Sausen, and L. Li, 2003: A comparison of climate response to different radiative forcings in three general circulation models: Towards an improved metric of climate change. *Climate Dyn.,* **20,** 843–854, doi:10.1007/s00382-003-0305-9.

Lu, J.-H., and M. Cai, 2009: A new framework for isolating individual feedback processes in coupled general circulation climate models. Part I: Formulation. *Climate Dyn.,* **32,** 873–885, doi:10.1007/s00382-008-0425-3.

——, and ——, 2010: Quantifying contributions to polar warming amplification in a coupled general circulation model. *Climate Dyn.,* **34,** 669–687, doi:10.1007/s00382-009-0673-x.

Manabe, S., 1983: Carbon dioxide and climate change. *Advances in Geophysics,* Vol. 25, Academic Press, 39–82.

——, and R. T. Wetherald, 1975: The effects of doubling the CO_2 concentration on the climate of a general circulation model. *J. Atmos. Sci.,* **32,** 3–15.

Mitchell, J. F. B., C. A. Wilson, and W. M. Cunnington, 1987: On CO_2 climate sensitivity and model dependence of results. *Quart. J. Roy. Meteor. Soc.,* **113,** 293–322.

Schneider, E. K., B. P. Kirtman, and R. S. Lindzen, 1999: Tropospheric water vapor and climate sensitivity. *J. Atmos. Sci.,* **56,** 1649–1658.

Suarez, M. J., and L. L. Takacs, 1995: Documentation of the Aries-GEOS dynamical core: Version 2. NASA Tech. Memo. 104606, 44 pp.